

Computational modelling of masonry with a view to Groningen induced seismicity

J.G. Rots, F. Messali, R. Esposito, S. Jafari & V. Mariani

Structural Mechanics, Civil Engineering & Geosciences, TU Delft, Delft, Netherlands

Paper submitted to and accepted for the Conference on Structural Analysis of Historical Constructions SAHC, to be held in Leuven, September 2016

ABSTRACT: Computational models for masonry are briefly reviewed and judged upon their practical performance at the structural scale, i.e. at building level, in a nonlinear pushover or nonlinear time history setting. Particular attention is given to an anisotropic macro model based upon total stress-strain relations in tension, shear and compression with proper unloading/reloading. A multi-level experimental campaign for Groningen masonry delivered material input and validation data at component and structural level. Brief attention is given to the temporal discretization, with a sequentially linear scheme that drives the solution over the peak up to structural softening down to zero, as an alternative to incremental-iterative implicit schemes.

1 INTRODUCTION

Seismic action and unreinforced masonry is a popular scientific as well as societally relevant theme in many countries worldwide. Recently, also The Netherlands started to face seismic risk, from man-made shallow earthquakes due to gas extraction in the province of Groningen. This poses serious problems. About 77% of the buildings stock in that region is unreinforced masonry, including aged and historical constructions. Houses and buildings have not at all been designed according to any seismic code, since the idea of earthquakes in the country could not be imagined. Masonry walls are extremely slender, with slenderness ratios equal to 25 (whereas 7 is usual in seismic countries). Reinforcement is absent. In cavity walls only weak and often corroded ties are present. Window openings are large, and stability systems often depend on slender piers only, spandrels being marginal, e.g. terraced houses with a through-room ('doorzonwoning'). Buildings are often loosely stacked, with little attention to stiffness of floors and diaphragms and to connections. Furthermore, the variety in building typologies, geometries, materials, state and age is large. This all in a setting of uncertain PGA maps that are regularly upgraded according to progressing insights from geologists and ground motion prediction communities. Eventually, the local population requires to assess in a short time whether their houses are safe, what type of upgrading is necessary, and whether damage from light earthquakes (over 20 quakes annually with magni-

tude 3.6 in Huizinge 2012 being the largest up till now) will be repaired and which costs covered.

In this context, the Nederlandse Aardolie Maatschappij (NAM), a combination of Shell, Exxon and Dutch government, initiated a comprehensive research program with experimental testing and computational modelling of masonry being one of the key topics to assess risk and fragility.

As unreinforced masonry systems respond highly nonlinear with quick dramatic changes in static and dynamic building properties, linear elastic procedures like lateral force methods or linear response spectrum analyses do not seem the way to go. Also, global ductility factors for the specific housing stock are not yet available. Consequently, the focus is on dynamic nonlinear time history analysis and/or nonlinear quasi-static pushover analysis. Figure 1 gives an impression of nonlinear FEM simulations for three typical buildings, two tested by EU Centre Pavia at a shake table (Graziotti et al. 2015, 2016) and one tested in cyclic pushover in Delft (Ravenshorst et al. 2016). Such studies require validated constitutive formulations and pragmatic discretization at the structural scale, i.e. most interest is in smeared continuum models and shell type representations.

2 OVERVIEW MASONRY MODELS

Numerous nonlinear modelling methods for masonry exist and can be categorized along different dimensions. One way of categorizing them is the following

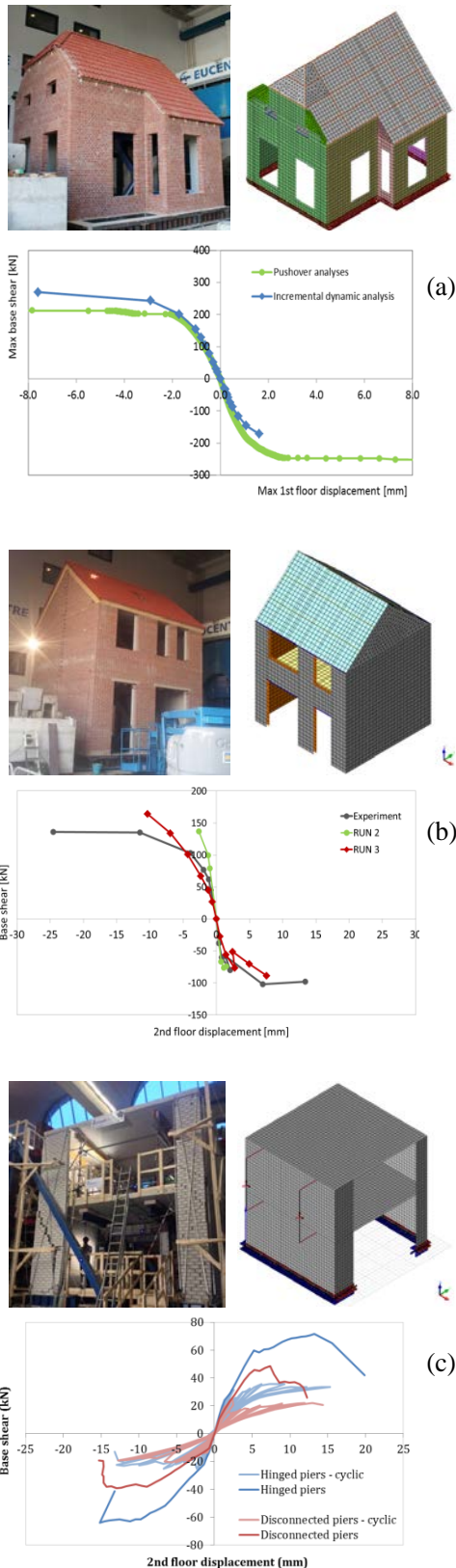


Figure 1. Examples of nonlinear time history and pushover analyses at building level, for 3 tested houses in NAM project.

(limited references to overview papers are included; further references can be found in those papers):

- Micro versus macro.

As masonry is an ordered material, either a detailed brick-to-brick modelling philosophy or a composite modelling approach where the masonry is conceived as an orthotropic continuum can be pursued. E.g.: Rots et al (1994), Lofti & Shing

(1994), Lourenco & Rots (1997, 1998), Gamba-rotta & Lagomarsino (1997).

- Discontinua versus continua.

Similarly, the nonlinear behavior can be either lumped into stress-displacement relations in interface elements at joints, or smeared out into stress-strain relations for the orthotropic continuum.

- FEM versus DEM.

The Discrete or Distinct Element Method was originally developed for rigid blocks with nonlinear contacts between them, later extended to deformable blocks. For applications to masonry and overview see e.g. Lemos (2007), Roca et al (2010), Smoljanovic et al (2015). Alternative names are rigid body spring models, or discontinuous deformation analysis. They come close to finite element models with interfaces, but often the solution process is different.

- Implicit versus Explicit.

Similar to the previous distinction. Finite element methods use an implicit solver that assembles the global stiffness matrix in all steps and pursues satisfaction of constitutive behavior and equilibrium. Instead, explicit finite element codes start from the theory of dynamics, and set up the equation of motion, marching forward explicitly with very small time steps, without assembling the global stiffness matrix, e.g. Dhanasekar & Haider (2008), Bakeer (2009), Giamundo et al (2014), while an early trial was made by Janssen reported in Rots et al (1994). Explicit codes are e.g. UDEC, LS-Dyna (applied by Arup in the NAM project), Abaqus-explicit, while implicit FEM codes are numerous. Explicit codes pose demands on time step size when large stiffness differences occur between elements. Also element erosion or removal criteria have to be set and viscosity may be overestimated. But their advantage is that they are very stable even after a series of adjacent elements fail. FEM codes do not have such restrictions, but conversely, post-peak they may suffer from convergence problems once softening proceeds and the stiffness may become ill-conditioned. For that reason, sequentially linear implicit FEM schemes were developed, but are still in an early stage (e.g. Rots & Invernizzi 2004).

- Macro beam/frame versus plane-stress/shell representations.

The former models reduce piers and spandrels to beam elements with calibrated component properties, while the latter start from (more) direct material properties and model the geometry directly. The advantage of the first is that only a limited number of degrees of freedom is required per building, while shell models are computationally demanding. On the other hand the latter include in-plane as well as out-of-plane failure modes, while out-of-plane modes for slender walls are of-

ten absent in beam/frame models (Penna, Lagomarsino & Galasco (2013).

- Multi-scale analysis, homogenization and enriched continua.

Masonry is a paradise for the multi-scale community. The often regular stacking pattern and periodicity allow for subdomains to be solved in a detailed manner in nested computational approaches. Also, the bond pattern suggests the use of higher order continua like micro-polar Cosserat or non-local or gradient damage theories. It is generally felt that these methods are not (yet) applicable in practical analysis at building level. A state-of-the-art was edited by e.g. Angellilo (2014), Lourenco & Milani (2014), Baraldi et al (2015).

- Decomposed-strain based versus total-strain based continuum models.

Many continuum models in implicit FEM codes start from the additive strain decomposition into an elastic part and a plastic/damage part, such as the multi-surface plasticity based approaches, e.g. Feenstra (1993), Lourenco et al (1997), Garafano et al (2015) with Rankine-Von Mises and Rankine-Hill; Milani & Valente (2015), Avossa & Malangone (2015) with Drucker-Prager elasto-plasticity; Pela et al (2012) with damage models. A disadvantage of such models is that they are not always robust, due to corners in the yield surface or complex anisotropic softening rules. For this reason, Feenstra et al (1998) started the development of total-strain based models in the FEM software DIANA. The new total stress is picked directly on the basis of the current total strain according to pre-set direct uniaxial stress-strain relations. This model developed for concrete is conceptually simple, robust and has become by far the most popular constitutive model in DIANA, at the structural scale too (Mendes & Lourenco 2009, Giamundo et al 2014, Giardina et al 2015). However, the current version of the model assumes initial isotropy and simple secant unloading/reloading, which calls for a new model including the specific features of masonry.

3 EXPERIMENTAL EVIDENCES

Due to the earthquakes induced in the province of Groningen, a comprehensive experimental campaign has been performed at the testing laboratory Stevin II at Delft University of Technology in 2015.

The campaign, with outcomes reported in Esposito et al. (2016), Jafari et al. (2016), Ravenshorst et al. (2016), and Ravenshorst & Messali (2016a,b), suggested that the following features should be considered when modeling structural masonry.

Masonry is an anisotropic material; besides, it presents preferential cracking planes, and the post-cracking behavior depends on the plane orientation.

Specifically, compressive tests performed normal to bed- and head-joints, respectively, returned different values of the Young's moduli and compressive strengths. Flexural tests with the moment vector parallel or orthogonal to the bed joints showed various failure crack patterns (Figure 2), to which significantly different tensile resistances are associated.

The compression tests showed a highly nonlinear behavior since very low stresses ($\sigma_c > 10\% f_c$).

Each single failure mechanism (tensile, compressive, and sliding failure) is characterized by different post-peak and unloading/reloading behaviors. The tensile behavior is described by quasi-brittle failure and secant unloading/reloading; compressed masonry showed larger ductility with a linear softening and elastic unloading down almost to zero compressive stresses (Fig. 3a); shear failure is characterized by quasi-brittle failure of cohesion, a long plastic plateau and elastic unloading (Fig. 3b).



Figure 2. Crack patterns of calcium silicate masonry specimens subject to: (a) out-of-plane vertical bending test; (b) out-of-plane horizontal bending test (Esposito et al., 2016).

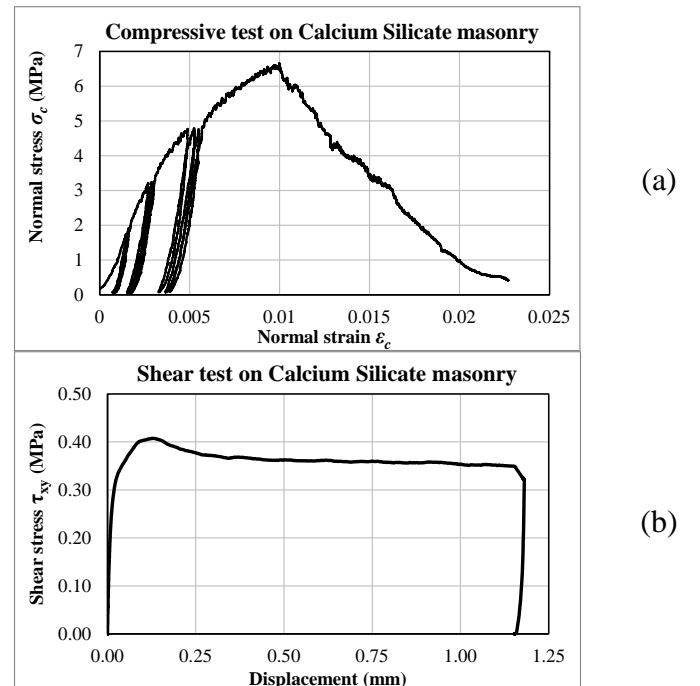


Figure 3. Examples of stress-strain and stress-displacement curves for compressive and shear tests, respectively, on Calcium Silicate Masonry (tests Esposito et al., 2016).

Both structural components and complex structures proved to be able to sustain displacement much

larger than that corresponding to the peak resistance; consequently, the definition of an algorithm procedure which may be stable also in the post-peak phase is essential to properly define the failure of the structure.

4 A NEW ANISOTROPIC TOTAL STRAIN MODEL

In order to properly reproduce the main characteristics of masonry under cyclic loading listed in the previous section, a constitutive model based on a simple smeared total strain formulation is hereinafter presented.

Traditional total strain based continuum models were originally developed for concrete and assume an isotropic material and are based on secant unloading and reloading; besides, they do not distinguish between tensile cracks (normal either to bed- or head-joints) and shear cracks. For these reasons, they might fail to accurately reproduce the different failure modes of masonry, and they usually underestimate the energy absorption.

The proposed constitutive model, conversely, covers tensile, shear and compression failure modes in a x,y horizontal-vertical bed joint-head joint system. Adequate secant, elastic and mixed hysteresis loops for the different failure modes are considered. Finally, the model includes the orthotropic behavior of masonry, by using different values for the elastic and inelastic properties in the two principal directions. The constitutive model can be applied in combination with regular plane stress (membrane) and curved shell elements for modelling either the in-plane or the out-of-plane failure of masonry structures.

Specifically, the model is characterized by the alignment of the x -local axis of each element with the mortar bed-joints, whereas the y -local axis is oriented along the head-joints (Figure 4).

In the elastic phase, anisotropy is considered. Poisson's ratio is set to zero for reasons of simplicity and robustness.

Three pre-defined crack directions in the plane of the element are considered: two of them are set along the local x - and y -axes of the element, whereas a third one (t) is aligned to the diagonal direction determined by the pattern of the bed- and head-mortar joints, as shown in Figure 4.

Different failure mechanisms are considered: tensile cracking, compressive crushing, and shear sliding. Tensile cracking is assessed in the three directions normal to the crack planes (i.e. local x -, y - and n -directions); a secant nonlinear unloading and reloading behavior, similar to that adopted in traditional total strain crack models, is assumed. Compressive crushing is assessed in the directions normal to the local x - and y -directions only (i.e.

normal to head- bed-joints, respectively); a nonlinear non-secant unloading and reloading behavior is considered. The in-plane shear stresses are limited by a standard Coulomb friction failure criterion, based on the stress normal to the bed-joint.

In shell elements, the out-of-plane shear stiffness components are assumed to be linear elastic.

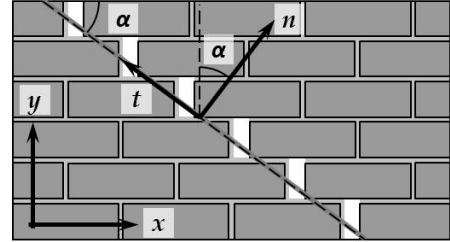


Figure 4. Pre-defined crack directions (x, y, n) included in the constitutive model.

4.1 Elastic behavior

The orthotropic behavior of masonry is one of the peculiar features of the proposed model. Different elastic parameters are set in the direction of the bed- and head-joints. In order to improve the stability of the numerical procedure, the model assumes that there is no coupling between the stiffness of the normal components in the x - and y -directions and that of the in-plane shear component; any interaction between the normal components is also neglected. The assumption appears to be adequate given the small values of the Poisson's ratio typical of Dutch brick masonry (Esposito et al., 2016) and the small role that the elastic behavior plays after that the masonry is cracked. As a consequence, the stiffness matrix is a diagonal matrix, whose components are reported in Equation (1).

$$\begin{Bmatrix} \sigma_{xx} \\ \sigma_{yy} \\ \sigma_{zz} \\ \tau_{xy} \\ \tau_{yz} \\ \tau_{zx} \end{Bmatrix} = \begin{bmatrix} E_x & 0 & 0 & 0 & 0 & 0 \\ 0 & E_y & 0 & 0 & 0 & 0 \\ 0 & 0 & E_z & 0 & 0 & 0 \\ 0 & 0 & 0 & G & 0 & 0 \\ 0 & 0 & 0 & 0 & G & 0 \\ 0 & 0 & 0 & 0 & 0 & G \end{bmatrix} \begin{Bmatrix} \varepsilon_{xx} \\ \varepsilon_{yy} \\ \varepsilon_{zz} \\ \gamma_{xy} \\ \gamma_{yz} \\ \gamma_{zx} \end{Bmatrix} \quad (1)$$

Three independent values (the Young's moduli E_x and E_y , and the shear modulus G), needs to be evaluated. The two Young's moduli E_x and E_y can be derived by standard compressive tests on masonry wallets, tested normally to bed- and head-joints, respectively. Whether other information is not available, the Young's modulus in the direction parallel to bed-joints might be set as a fraction of the modulus normal to bed-joints. Based on the experimental results reported in (Jafari et al. 2016), the values in Table 1 are proposed.

The shear modulus G can be evaluated from diagonal compressive tests, as suggested by standards (ASTM International, 2010), or it can be simply es-

timated as a fraction of the Young's modulus. Standards (de Normalisation C. E., 2005) suggest that the shear modulus, G , may be taken as 40 % of the Young's modulus normal to bed-joints, E_y . However, experiments (e.g. Bosiljkov et al, 2005) show that the value of the shear modulus can be significantly reduced (10-30% of the elastic modulus).

Table 1. Estimated ratios between the Young's moduli in x - and y -directions.

E_x/E_y	Existing masonry	Replicated masonry
Clay bricks	0.45 (solid bricks)	0.77 (perforated bricks)
Calcium silicate bricks	0.7	0.63

4.2 Tensile behavior normal to the local axes (x, y)

In the element local x - and y -directions, positive tensile stresses are computed according to an uniaxial relation, based on the respective strain component (ε_i), the value of the maximum strain that has ever been experienced during the loading history (ε_{ti}) and the corresponding stress (σ_{ti}), where i takes the value 1 for the x -direction, and 2 for the y -direction.

The tensile uniaxial stress-strain curve for each local direction is defined by the Young's modulus (E_i), the tensile strength (f_{ti}), and the crack fracture energy (G_{fii}) (Fig. 5). A linear softening curve is assumed, and the ultimate tensile strain (ε_{uti}) defined as the strain value at which the crack is fully open and no stress can be transferred. Consequently, ε_{uti} can be computed according to the following equation:

$$\varepsilon_{uti} = 2G_{fii} / (hf_{ti}) \quad (2)$$

where h is the crack bandwidth of the element, over which the crack is smeared, related to the size of the finite element. Secant unloading and reloading is assumed.

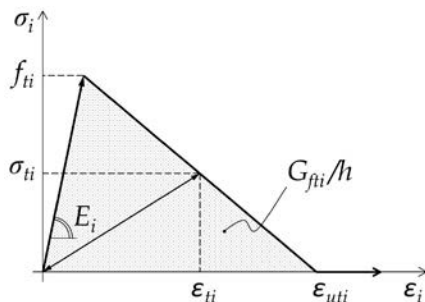


Figure 5. Uniaxial tensile stress-strain curve normal to the local axes (x, y).

The tensile strength parallel to bed-joints (f_{tl}) is evaluated in each single integration point and depends on analytical observations of the behavior of masonry in tension initially recorded by Kasten & Schubert (1985), and commonly accepted in the literature (e.g. Rots 1997). If head-joints are assumed to be unable to transfer any tensile strength, masonry failure can occur when either bricks fail in tension

(mechanism a), or shear slip takes place along the bed-joints (mechanism b). Thus, the masonry tensile strength parallel to bed-joints (f_{tl}) can be computed according to the following set of equations:

$$f_{tl} = \min(f_{tl,a}; f_{tl,b}) \quad (3)$$

$$f_{tl,a} = \frac{h_b}{2(h_b + h_j)} f_{tb} \quad (4)$$

$$f_{tl,b} = \frac{\tau_{\max}}{\tan \alpha} \quad (5)$$

where $f_{tl,a}$ and $f_{tl,b}$ are the tensile strengths related to mechanism a and b , respectively, h_b and h_j the thickness of bricks and bed-joints, respectively, and τ_{\max} is the limit shear stress (completely defined in section 4.4).

The tensile strength normal to bed-joints (f_{t2}) is a fix input value, and can be estimated from flexural tests on masonry wallets with the moment vector parallel to the bed joint and in the plane of the wall.

The same value for the fracture energy is assumed for both the loading directions.

4.3 Compressive behavior normal to the local axes (x, y)

In the element x - and y -direction, the normal compressive stresses are defined by the respective strain component (ε_i), the minimum value of the strain that has ever been reached (ε_{ci}), and the corresponding stress (σ_{ci}), where i takes the value 1 for the x -direction, and 2 for the y -direction.

The compressive uniaxial stress-strain curve for each local direction is defined by the Young's modulus (E_i), the compressive strength (f_{ci} , defined as positive value), the compressive fracture energy (G_{fci}), and a factor (n_i) which takes into account the deformability of the masonry beyond the elastic limit and is defined as:

$$n_i = (E_i \varepsilon_{pi}) / f_{ci} \quad (6)$$

where ε_{pi} is the strain of masonry at peak compressive strength and is defined as positive value.

The uniaxial curve consists of a sequence of a third order and a parabolic curve up to the compressive strength, and a linear softening curve until a residual stress of 10% of the compressive strength is reached:

$$\sigma_i = \begin{cases} -\min\left(0.1; -\frac{\varepsilon_i - \varepsilon_{uci}}{\varepsilon_{pi} + \varepsilon_{uci}}\right) f_{ci} & \varepsilon_i < \varepsilon_{pi} \\ B_{1i} \varepsilon_i^2 + 2\varepsilon_{pi} B_{1i} \varepsilon_i + f_{ci} + \varepsilon_{pi}^2 B_{1i} & -\varepsilon_{pi} \leq \varepsilon_i < -\frac{f_{ci}}{E_i} \\ B_{2i} \varepsilon_i^3 + B_{3i} \varepsilon_i^2 - E_i \varepsilon_i & -\frac{f_{ci}}{E_i} \leq \varepsilon_i < 0 \end{cases} \quad (7)$$

where B_1 , B_2 and B_3 are defined as follows:

$$B_{1i} = \frac{\sqrt[3]{n_i} - 1}{\sqrt[3]{n_i}} \left[\frac{E_i (\varepsilon_{pi} - \varepsilon_i)}{E_i \varepsilon_{pi} - \varepsilon_{uci}} \right]^2 - 1 \quad (8)$$

$$B_{2i} = \left(\frac{\sqrt[3]{n_i} - 2}{\sqrt[3]{n_i}} + 2 \frac{\sqrt[3]{n_i} - 1}{\sqrt[3]{n_i}} \cdot \frac{f_{ci}}{E_i \varepsilon_{pi} - f_{ci}} \right) \left(\frac{E_i}{f_{ci}} \right)^3 \quad (9)$$

$$B_{3i} = \left(\frac{3 - 2\sqrt[3]{n_i}}{\sqrt[3]{n_i}} + 2 \frac{\sqrt[3]{n_i} - 1}{\sqrt[3]{n_i}} \cdot \frac{f_{ci}}{E_i \varepsilon_{pi} - f_{ci}} \right) \left(\frac{E_i}{f_{ci}} \right)^2 \quad (10)$$

and the ultimate compressive strain (ε_{uci}) is defined as the absolute value of the strain for which the linear softening curve would reach the zero-stress level, according to the following formulation:

$$\varepsilon_{uci} = \varepsilon_{pi} + \max \left[0; \frac{2G_{fci}}{h f_{ci}} - \frac{f_{ci}}{E_i \sqrt[3]{(n_i)^2}} - \frac{\sqrt[3]{n_i} + 1}{\sqrt[3]{n_i}} \left(\varepsilon_{pi} - \frac{f_{ci}}{E_i} \right) \right] \quad (11)$$

where h is the crack bandwidth of the element. For sake of simplicity and given the uncertainties related to the evaluation of the compressive fracture energy G_{fci} , Equation 11 assumes that the curve is approximated by a multilinear curve.

A bilinear unloading curve is proposed and an unloading factor λ ($0 \leq \lambda \leq 1$) is defined: elastic unloading (unloading stiffness E_i) is followed by secant unloading according to:

$$\sigma_i = \begin{cases} \sigma_{ci} + E_i (\varepsilon_i - \varepsilon_{ci}) & \varepsilon < \varepsilon_{ci} - (1 - \lambda) \frac{\sigma_{ci}}{E_i} \\ \frac{\lambda}{1 - \lambda} E_i \varepsilon_i & \varepsilon_{ci} - (1 - \lambda) \frac{\sigma_{ci}}{E_i} \leq \varepsilon < 0 \end{cases} \quad (12)$$

Consequently, $\lambda = 0$ corresponds to unloading to zero stress with the initial stiffness E_i and $\lambda = 1$ corresponds to secant unloading to the origin.

A secant reloading is also assumed:

$$\sigma_i = \sigma_{0i} + \frac{\Delta \varepsilon_i}{\varepsilon_{ci} - \varepsilon_{0i}} (\sigma_{ci} - \sigma_{0i}) \quad (13)$$

where $\Delta \varepsilon_i$ is the strain increment, and ε_{0i} and σ_{0i} are the strain and stress at the beginning of the increment, respectively.

The uniaxial compressive stress-strain curve from Equations 7-13 is graphically displayed in Figure 6.

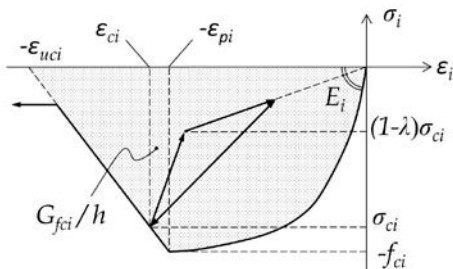


Figure 6. Uniaxial compressive stress-strain curve normal to the local axes (x , y).

The proposed model proved to be capable to reproduce properly the highly nonlinear compressive behavior showed by performed tests reported in Jafari et al. (2016) and Esposito et al. (2016); this specific feature is required to describe the energy dissipation that can occur also before that the peak strength is reached. An example of a comparison between the stress-strain curves obtained from the compression tests on Calcium Silicate masonry performed normal to bed-joints and the numerical curve obtained from Equation 7 is show in Figure 7.

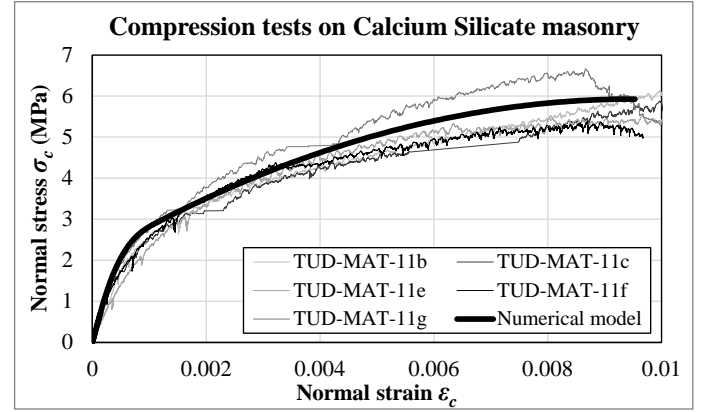


Figure 7. Stress-strain curves up to peak strength from compression tests on Calcium Silicate masonry performed normal to bed-joints (Esposito et al. 2016) and from Equation 7 (absolute values are considered).

4.4 In-plane shear behavior along the mortar joints

An elastic uniaxial stress-strain curve depending on the initial shear stiffness (G) and a limit cap (τ_{max}), relates the in-plane shear stress (τ_{xy}) and the in-plane shear strain (γ_{xy}):

$$\tau_{xy} = \begin{cases} -\tau_{max} & \tau_0 + G\Delta\gamma_{xy} < -\tau_{max} \\ \tau_0 + G\Delta\gamma_{xy} & -\tau_{max} \leq \tau_0 + G\Delta\gamma_{xy} \leq \tau_{max} \\ \tau_{max} & \tau_0 + G\Delta\gamma_{xy} > \tau_{max} \end{cases} \quad (14)$$

where $\Delta\gamma_{xy}$ is the strain increment, τ_0 is the stress at the beginning of the increment, and τ_{max} is defined according to the following frictional law:

$$\tau_{max} = \max(0; c - \sigma_{yy} \tan \varphi) \quad (15)$$

where c is the cohesion and φ the friction angle.

The cohesion c reduces linearly with the cumulative frictional shear strain γ_{cum} until its value is reduced to zero at a total shear strain of $\gamma = \gamma_{ult}$. Besides, when an integration point has already cracked normal to the horizontal direction ($\varepsilon_{t2} > f_{t2} / E_2$) the cohesion c is immediately reduced to zero. γ_{cum} is defined as the sum of the incremental shear strains over all steps in which the shear stress is equal to the limit cap ($|\tau| = \tau_{max}$). γ_{ult} is defined by the shear fracture energy (G_{fs}) as:

$$\gamma_{ult} = \frac{2G_{fs}}{h} + \frac{\sigma_{yy} \tan \varphi}{G} \quad (16)$$

where h is the crack bandwidth of the element.

Figure 8 illustrates graphically Equations 14-16.

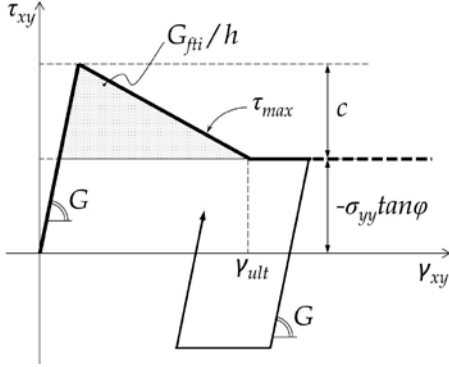


Figure 8. Uniaxial in-plane shear stress-strain curve.

4.5 Tensile behavior normal to the diagonal axis n

A non-linear uniaxial behavior of the tensile stresses normal to the diagonal failure line defined by the angle α is also considered.

The state of stress in the coordinate system nt , rotated of an angle β with respect to the local xy axes ($\beta = \pi/2 \pm \alpha$), is computed according to equation 17.

$$\begin{Bmatrix} \sigma_{nn} \\ \sigma_{tt} \\ \tau_{nt} \end{Bmatrix} = \begin{bmatrix} \frac{1 + \cos 2\beta}{2} & \frac{1 - \cos 2\beta}{2} & -\sin 2\beta \\ \frac{1 - \cos 2\beta}{2} & \frac{1 + \cos 2\beta}{2} & \sin 2\beta \\ -\frac{\sin 2\beta}{2} & \frac{\sin 2\beta}{2} & \cos 2\beta \end{bmatrix} \begin{Bmatrix} \sigma_{xx} \\ \sigma_{yy} \\ \tau_{xy} \end{Bmatrix} \quad (17)$$

A tensile cap for the normal stress σ_{nn} is considered. The cap is evaluated via a quadratic relation between the tensile resistance in the x - and the y -direction:

$$f_{ta} = \frac{f_{tx} \cdot f_{ty}}{\sqrt{(f_{tx} \cos \alpha)^2 + (f_{ty} \sin \alpha)^2}} \quad (18)$$

where f_{tx} and f_{ty} are evaluated according to the procedure reported in section 4.2.

If the ratio coefficient σ_{nn} / f_{ta} is larger than one, then the stresses in the local xy coordinates are recomputed so that the component in the n -direction is equal to the tensile cap; the other components (σ_{tt} and τ_{nt}) are unchanged:

$$\begin{Bmatrix} \sigma_{xx} \\ \sigma_{yy} \\ \tau_{xy} \end{Bmatrix} = \begin{bmatrix} \frac{1 + \cos 2\beta}{2} & \frac{1 - \cos 2\beta}{2} & \sin 2\beta \\ \frac{1 - \cos 2\beta}{2} & \frac{1 + \cos 2\beta}{2} & -\sin 2\beta \\ \frac{\sin 2\beta}{2} & -\frac{\sin 2\beta}{2} & \cos 2\beta \end{bmatrix} \begin{Bmatrix} f_{ta} \\ \sigma_{tt} \\ \tau_{nt} \end{Bmatrix} \quad (19)$$

It should be noted that the diagonal strength calculated according to Equation 18 is deeply related to

the masonry shear sliding mechanism, since the considered tensile strength in the x -direction is reached when slip takes place along the bed-joints (section 4.2). Alternatively, the diagonal tensile strength can be estimated via diagonal compression tests, as widely suggested in the literature (e.g Calderini et al., 2010). The diagonal compression tests return a single value of the tensile strength, independent of the confining effect provided by the vertical stresses. However, as displayed in Figure 9, the values of the computed diagonal resistance are almost constant as long as a small compression is provided along the vertical axis.

Since both the diagonal cracking failure mode and the shear behavior along the bed-joints failure mode are strictly related to masonry shear sliding, the proposed model can evaluate Equations 17-19 either additionally or alternatively to Equations 14-16.

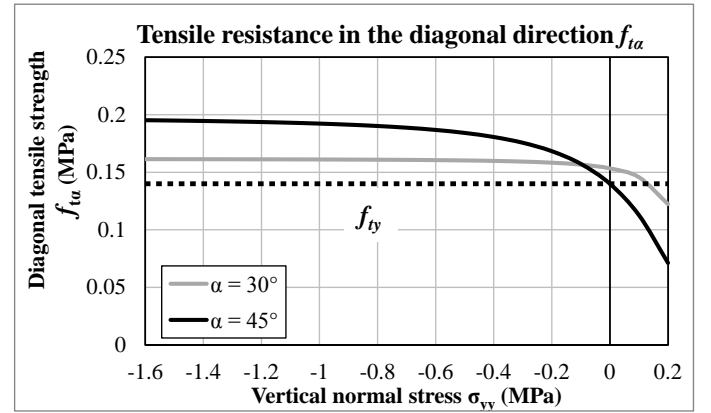


Figure 9. Tensile strength in the diagonal direction at varying the vertical normal stress for typical brick masonry patterns ($\alpha = 30^\circ; 45^\circ$).

5 NUMERICAL EXAMPLES

The ability of the proposed model to reproduce the outcomes of experimental results performed on masonry structural components is hereinafter discussed. Four numerical analyses of masonry walls subjected to in-plane cyclic loads (two from the literature and two from the recent experimental campaign performed at TU Delft in 2015) are presented. The walls are modelled with eight-node continuum plane stress elements with average edge length of 0.1 m. A quasi-static implicit non-linear analysis is performed with full New-Raphson iteration scheme, taking both physical and geometrical nonlinear (Total Lagrange) behavior into account. Both the displacement and force based convergence criterion are applied with standard tolerance values (0.01).

In the implemented constitutive model the diagonal cracking criterion is considered as an alternative to shear friction criterion (i.e. Equations 14-16 are not considered).

5.1 CNR walls

Two masonry walls were tested at Pavia University, Italy, in an international cooperative program.

Both walls were composed of $250 \times 120 \times 55 \text{ mm}^3$ bricks, arranged in two-wythes, of same width (1000 mm), thickness (250 mm), and joint thickness (10 mm). Two different height/width ratio (2.0 and 1.35) were chosen, to obtain a flexural (for the high wall) and shear failure mechanisms (for the short wall).

The loads and boundary conditions are chosen in order to reproduce properly the experimental conditions. First, the dead load and a uniform pressure load of 0.6 N/mm^2 are applied on the top edge. Subsequently, the vertical load is maintained constant and a series of prescribed horizontal displacements of increasing amplitude is imposed at the top-left corner. All nodes at the top edge are rigidly linked to have the same vertical and horizontal displacements.

Figure 10 presents a comparison between the experimental and numerical results of the high wall in terms of horizontal force vs. top displacement. Figure 11 shows the principal tensile strains represented on the deformed mesh for the maximum and minimum lateral displacement ($\pm 12.5 \text{ mm}$). The output of the numerical response shows the rocking failure mechanism of the wall, with flexural horizontal cracks at the top and bottom ends that cyclically opens and closes according to the loading verse (Figure 11). A similar crack pattern was observed during the experimental test, as roughly depicted in the inset in Figure 10 and reported in (Anthoine et al. 1995). Also the peak resistance ($F_{num} = 65.4 \text{ kN}$ vs. $F_{exp} = 72 \text{ kN}$) and the low energy dissipated are quite accurately predicted by the numerical simulation.

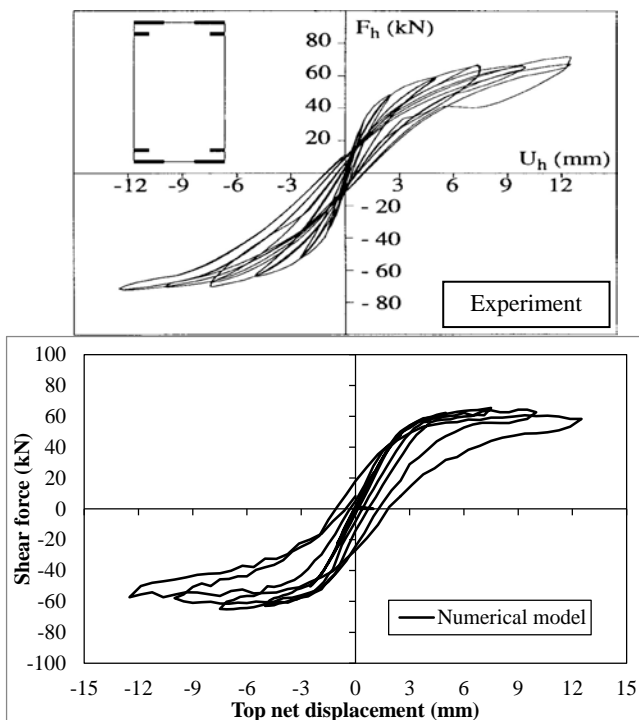


Figure 10. Experimental (from Anthoine et al 1995) and numerical shear force–displacement diagram of the CNR high wall.

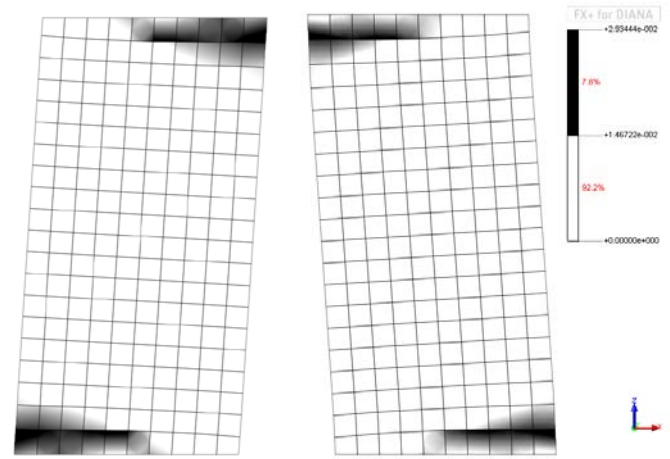


Figure 11. Principal tensile strains on the deformed mesh at the maximum positive and negative displacements, respectively, of the CNR high wall.

Similar remarks can be stated regarding the low wall. Figure 12 reports the horizontal force vs. top displacement plot for both the experimental test and the numerical simulation. The numerical analysis can provide an accurate prediction of the peak resistance ($F_{num} = 80.5 \text{ kN}$ vs. $F_{exp} = 84 \text{ kN}$) and a good description of the post-peak softening behavior exhibited by the short wall. Besides, also the large energy dissipation associated to shear failure is fairly predicted.

5.2 TUD walls

As stated in Section 3, a series of masonry shear walls has been tested within the framework of the experimental campaign performed at Delft University of Technology (Ravenshorst & Messali 2016a).

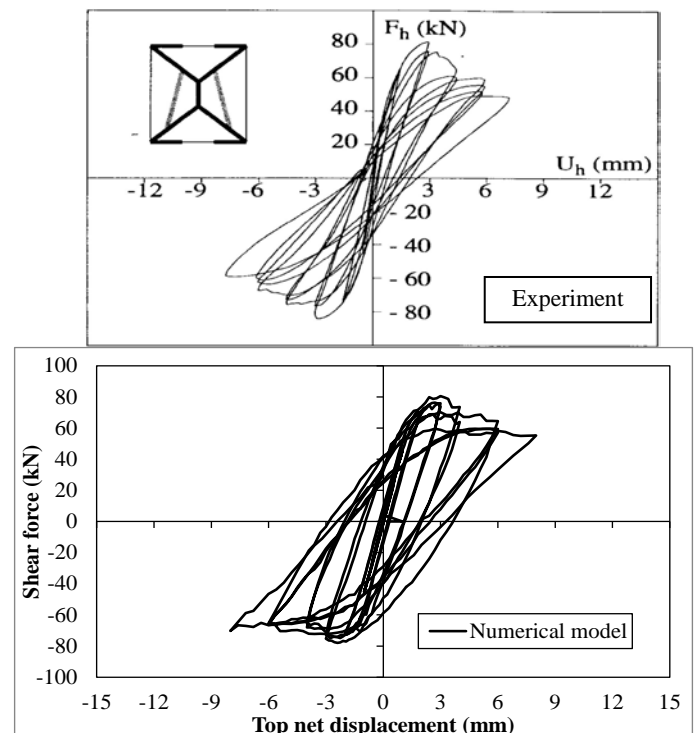


Figure 12. Experimental (from Anthoine et al 1995) and numerical shear force–displacement diagram of the CNR short wall.

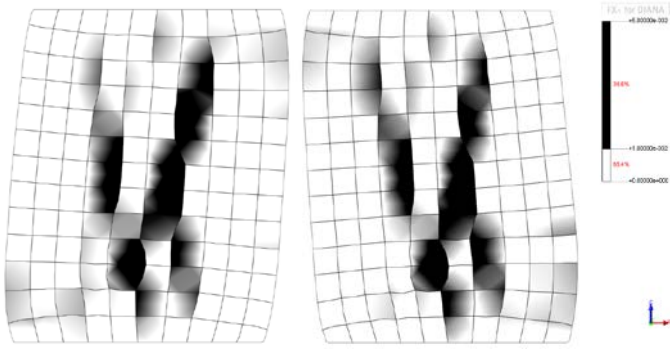


Figure 13. Principal tensile strains on the deformed mesh at the maximum positive and negative displacements, respectively, of the CNR short wall.

The experimental campaign included four “short walls” (with shear ratio $H/L = 2.5$) and three “long walls” ($H/L = 0.6875$). In this paper, one short wall (TUD_COMP-0a) and one long wall (TUD_COMP-4) are considered. Both walls were composed of $210 \times 102 \times 70 \text{ mm}^3$ calcium silicate bricks, arranged in a single-wythe, with same height (2750 mm), thickness (102 mm), and joint thickness (10 mm). The short wall was 1.1 m long, whereas the long wall was 4.0 m long, so that both flexural (for the high wall) and shear failure mechanisms (for the short wall) are considered. The numerical loads and boundary conditions are chosen in order to reproduce properly the experimental conditions. In the first load-step the dead load and a uniform pressure load on the top edge of the wall (of 0.7 N/mm^2 and 0.5 N/mm^2 , respectively) are applied. In the following steps the vertical load is maintained constant and a series of prescribed horizontal displacement of increasing amplitude is imposed at the top-left corner of the wall. All the points of the top edge of the wall are rigidly linked to have the same vertical and horizontal displacements.

Figure 14 presents a comparison between experimental and numerical results of the short wall in terms of horizontal force vs. top displacement. The peak lateral resistance is accurately predicted ($F_{num} = 29.5 \text{ kN}$ vs. $F_{exp} = 30.6 \text{ kN}$); however, the energy dissipation is underpredicted for most of the cycles of large amplitude.

Figure 15 shows a comparison between the crack pattern at the end of the experimental test and the principal tensile strains represented on the deformed mesh for the minimum lateral displacement (-22.5 mm). The output of the numerical response shows that a rocking mechanism occurs, with flexural horizontal cracks at the top and bottom ends of the wall; however, both the experimental crack pattern and the numerical output show that also diagonal cracking takes place in the panel.

The numerical simulation of the long wall returns more inaccurate results. Figure 16 presents a comparison between experimental and numerical results of the short wall in terms of horizontal force vs. top displacement. The peak lateral resistance is over

predicted ($F_{num} = 160 \text{ kN}$ vs. $F_{exp} = 123 \text{ kN}$) and also the energy dissipation is under predicted for most of the cycles of large amplitude. Finally, also the comparison between the crack pattern at the end of the experimental test and the principal tensile strains represented on the deformed mesh for the minimum lateral displacement (-5.4 mm) shows some discrepancies (Figure 17), even if the detected main failure mechanism is the same (diagonal cracking with dissipating shear failure). The output of the numerical response shows the incipience of a rocking mechanism, and diffuse diagonal inelastic strains in the middle of the wall panel, whereas, only localized diagonal cracks are detected from the experimental test.

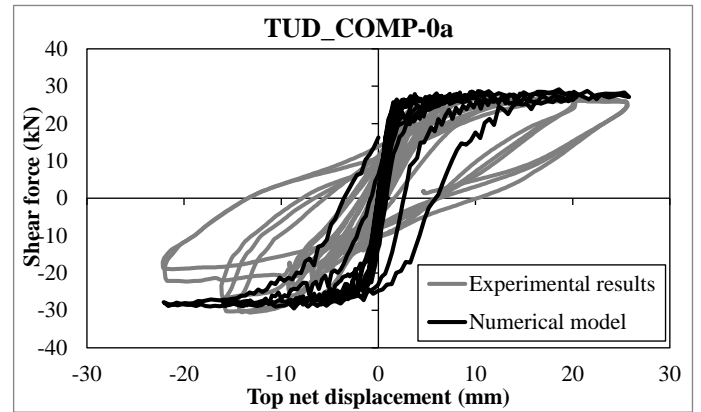


Figure 14. Experimental (from Ravenshorst & Messali 2016a) and numerical shear force–displacement diagram of the TUD short wall TUD_COMP-0a.

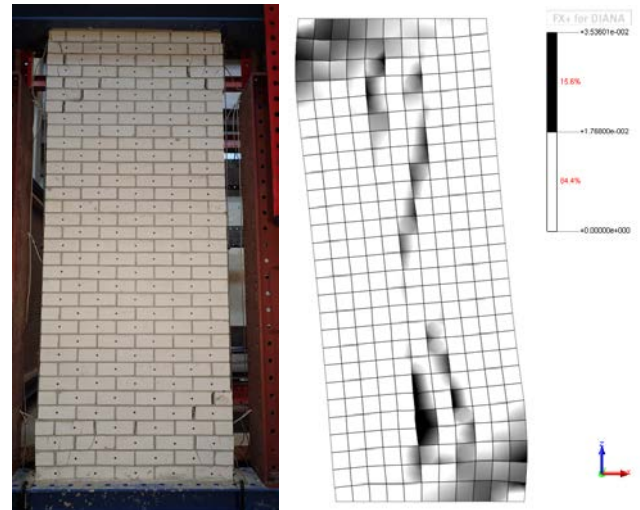


Figure 15. Experimental crack pattern at end stage and principal tensile strains on the deformed mesh at the maximum negative displacement, of the TUD short wall TUD_COMP-0a.

Therefore, the constitutive model appears to be able to reproduce adequately the experimental cyclic response of walls subjected either mainly to rocking failure (such as the CNR high wall and the TUD short wall) or to shear failure (such as the CNR low wall), in terms of resistance, and description of the hysteresis cycles. Moreover, the model is able to predict the post-peak softening behavior without experiencing stability issues. However the model still

needs to be improved further to provide more accurate results in terms of localization of the cracks and prediction of the energy dissipation (such as for the TUD long wall).

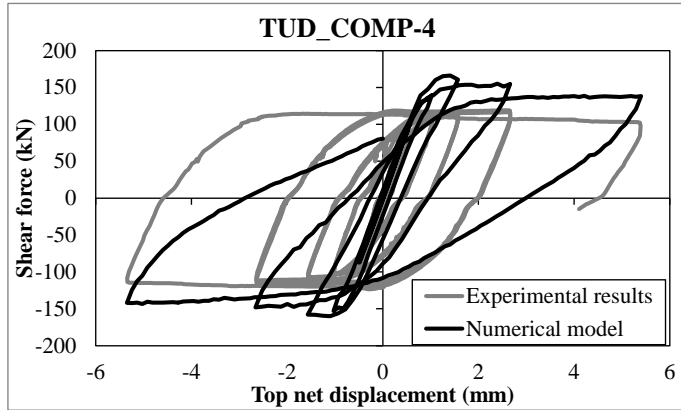


Figure 16. Experimental (from Ravenshorst & Messali 2016a) and numerical shear force–displacement diagram of the TUD long wall TUD_COMP-4.

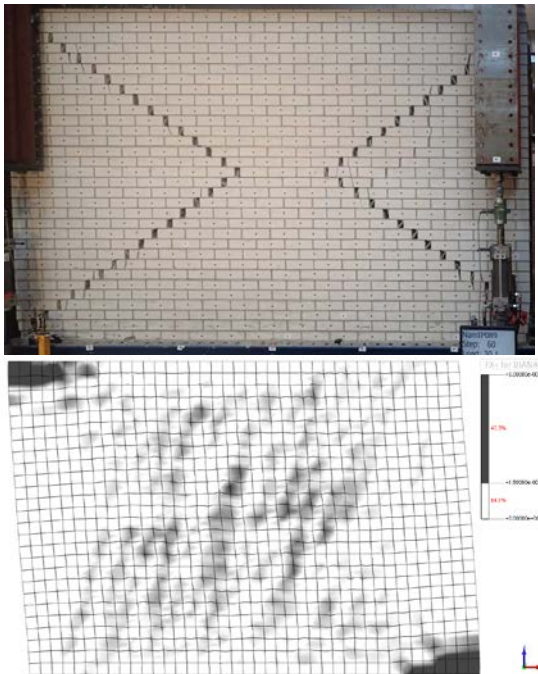


Figure 17. Experimental crack pattern at end stage and principal tensile strains on the deformed mesh at the maximum negative displacement, of the TUD long wall TUD_COMP-4.

6 SEQUENTIALLY LINEAR ANALYSIS (SLA)

Apart from the constitutive model and the finite element discretization, also the *temporal* discretization is key in tracing the nonlinear response of historical constructions. Usually analysts employ an incremental-iterative implicit procedure, but stability cannot always be guaranteed once structural parts start softening.

The issue was introduced in section 2, where the alternative of an explicit procedure with small time steps was mentioned so that motion information from an element does not go further than the immediately adjacent elements, circumventing the need to

set up a global stiffness matrix. In Section 2, also another alternative, namely sequentially linear implicit analysis was introduced, which will be further discussed in this section.

Masonry is a brittle softening material generating highly discontinuous load-displacement response with local peaks, jumps and snaps a structural level. In addition, upon applying finite load increments a series of Gauss points may crack simultaneously, leading to alternative equilibrium states (bifurcations) with multiple cracks competing to survive. The consequence is that incremental-iterative techniques cannot guarantee convergence and robustness due to negative softening tangent stiffness. Newton-Raphson does not fit such non-smooth temporal problems and advanced path-following techniques such as arc-length methods only partly remedy the problem. Some problems can be run in displacement control which is relatively stable, but in general cases like mass-proportional pushovers arc-length should be inserted which only partially helps. As a solution, sequentially linear analysis (e.g. Rots & Invernizzi 2004) has been developed. The method discretizes the local softening diagram (Figure 18) and traces global response via a series of critical events that reach some peak of some saw-tooth in some material point. After a material point has been critical, its strength and stiffness are reduced i.e. the secant stiffness is reduced, the linear analysis is repeated and the next critical event is searched for. The sequence of linear shots provides the global load-displacement response.

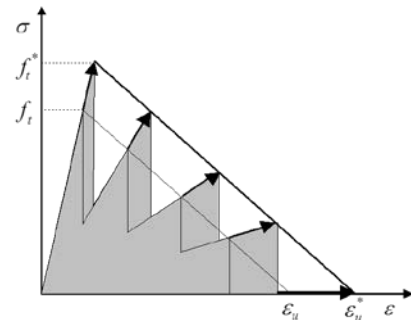


Figure 18. Saw-tooth softening diagram for SLA.

As the secant stiffness is always positive, the method is very stable, no ill-conditioning occurs and the process marches forward explicitly, even for spiky sharp snap-back type paths. The philosophy of the method is: we discretize the space via finite elements, we discretize the input material softening (saw-tooth) and we re-compute/scale the load from the fact that only one event occurs, i.e. only one new saw-tooth damage extension. Conventional models discretize the load in steps and the material point may be anywhere on a continuous softening branch. The SLA procedure is thus damage-driven, rather than load or time step driven. Extensions to non-proportional loading (DeJong et al 2008, Hendriks & Rots 2013, Van de Graaf 2016) where the existing load should be kept fixed and the active load scaled

and to stepwise rotating smeared cracks (Rots & Hendriks 2015) have been pointed out.

Figure 19 shows an example of the ETH Zurich wall, simulated before by e.g. Lourenco & Rots (1998). Both the tensile and compressive stress-strain curves of the masonry were discretized into saw-tooth diagrams. No attempt was made to fit parameters precisely. More than 25000 elastic cycles were run, and the series produced a stable load-displacement diagram far beyond the peak, even while significant energy was released in compressive softening.

A second example is a shear wall with a saw-tooth implementation for Coulomb friction with cohesion softening as well as tensile softening in interface elements. Again, the series of linear analyses produces as an envelope the nonlinear structural response (Figure 20). Here, compression softening was not included.

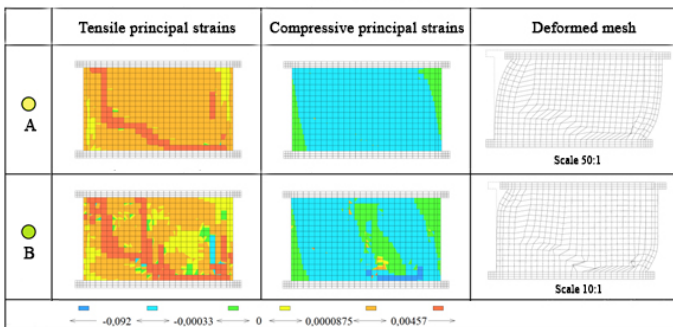
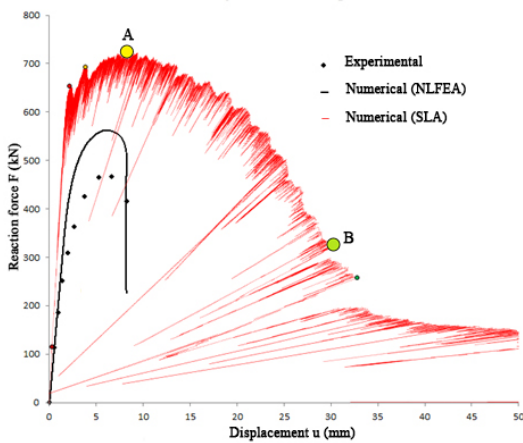


Figure 19. Load-displacement response and crack/crush zones for SLA analysis of ETH Zurich wall (Kraus 2014), compared to experiments and previous analysis (Lourenco & Rots 1998).

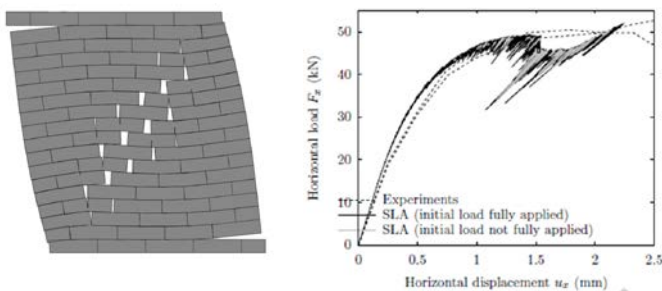


Figure 20. Load-displacement response and deformed mesh for SLA analysis of shear wall (Van de Graaf 2016).

Other examples for a masonry structure subjected to tunnelling-induced settlements, again with non-proportional loads, were reported by Giardina et al

(2013). A current limitation of SLA is that it is not possible to include cyclic response, only monotonic push-overs. This is currently under investigation, as is extension to geometrically nonlinear analysis (re-starts from the new mesh position, or via an updated B-matrix) and the possibility of sequentially linear response spectrum analysis.

CONCLUSION

Computational models for masonry were reviewed and judged upon their practical ability to predict failure, ductility and softening at structural level. A stress-total strain based anisotropic model was formulated including basic mechanisms in tension, shear and compression and adequate unloading/reloading. Validation against benchmarks available in the literature and a multi-level experimental campaign for Groningen masonry (typical result in Figure 21) demonstrated that the model is able to predict ultimate loads, ductility and structural hysteresis properly. Predicted crack directions replicate experimental findings but in some cases the patterns are too diffuse, which calls for improvements. Finally, the potential of sequentially linear analysis with saw-tooth softening is demonstrated to be a robust alternative to Newton-Raphson incremental-iterative schemes in implicit FEM, being able to capture structural softening in a stable way.



Figure 21. Example of experimental tensile, shear and compression (splitting) modes (Ravenshorst & Messali 2016a) to be reproduced numerically.

ACKNOWLEDGEMENT

A major part of this research was funded by NAM under contract number UI46268 “Physical testing and modelling – Masonry structures Groningen”, which is gratefully acknowledged, as the cooperation with Eucentre and Arup in this programme. The total-strain based masonry model was developed in cooperation between TU Delft and TNO DIANA BV. The implementation of the model into the DIANA development version and product version 10.1 was carried out by TNO DIANA BV, which is gratefully acknowledged.

REFERENCES

- Angelillo, M. (Ed.) 2014. *Mechanics of masonry structures*. Vienna: Springer.
- Anthoine, A., Magonette, G., Magenes, G. 1995. Shear-compression testing and analysis of brick masonry walls. In *Proceedings of the 10th European conference on earthquake engineering*. Rotterdam: Balkema.
- Avossa, A.M., Malangone, P. 2015. Seismic performance assessment of masonry structures with a modified “concrete” model. *Bull. Earthquake Eng.* 13, 2693-2718.
- ASTM International. 2010. ASTM E519 / E519M - 10. Standard Test Method for Diagonal Tension (Shear) in Masonry Assemblages. West Conshohocken, PA.
- Bakeer, T. 2009. Collapse analysis of masonry structures under earthquake actions. *Dissertation*, 262 pp., TU Dresden.
- Baraldi, D., Cecchi, A., Tralli, A. 2015. Continuous and discrete models for masonry like material: A critical comparative study. *Eur. Journal Mech. A/Solids* 50, 39-58.
- Bosiljkov, V. Z., Totoev, Y. Z., Nichols, J. M. 2005. Shear modulus and stiffness of brickwork masonry: an experimental perspective. *Struct. Eng. Mech.*, 20(1), 21-44.
- Calderini, C., Cattari, S., Lagomarsino, S. 2010. The use of the diagonal compression test to identify the shear mechanical parameters of masonry. *Constr. Build. Mater.*, 24(5): 677-685.
- DeJong, M.J., Hendriks, M.A.N., Rots, J.G. 2008. Sequentially linear analysis of fracture under non-proportional loading. *Eng. Fract. Mech.* 75, 5042-5056.
- Dhanasekar, M., Haider, W. 2008. Explicit finite element analysis of lightly reinforced masonry shear walls. *Comp. & Struct.* 86(1), 15-26.
- Esposito, R., Messali, F., Crielaard R., Rots, J.G. 2016. Tests for the material characterization of replicated masonry and wall ties, *Final Report*, Delft University of Technology.
- Feenstra, P.H. 1993. Computational aspects of biaxial stress in reinforced concrete. *PhD Thesis*, TU Delft.
- Feenstra, P.H., Rots, J.G., Arnesen, A. Teigen, J.G., Hoiseth, K.V. 1998. A 3D constitutive model for concrete based on a co-rotational concept. In: Proc. Euro-C Conference *Computational Modelling of Concrete Structures*, Balkema.
- Gambarotta, L., Lagomarsino, S. 1997. Damage models for the seismic response of brick masonry shear walls. Part I: the mortar joint model and its applications. *Earth. Eng. Struct. Dyn.* 26, 423-439.
- Garafano, A., Ceroni, F., Pecce, M. 2016. Modelling of the in-plane behavior of masonry walls strengthened with polymeric grids embedded in cementitious mortar layers. *Composites Part B* 85, 243-258.
- Giardina, G., Van de Graaf, A.V., Hendriks, M.A.N., Rots, J.G., Marini, A. 2013. Numerical analysis of a masonry facade subject to tunnelling-induced settlements. *Eng. Struct.* 54, 234-247.
- Giamundo, V., Sarhosis, V., Lignola, G.P., Sheng, Y., Manfredi, G. 2014. Evaluation of different computational modelling strategies for the analysis of low strength masonry structures. *Eng. Struct.* 73, 160-169.
- Graaf, A.V. van de (2016). Sequentially linear analysis for simulating brittle failure. PhD thesis, TU Delft, in press.
- Graziotti, F., Tomassetti, U., Rossi, A., Kallioras, S., Mandirola, M., Penna, A., Magenes, G. 2015. Experimental campaign on cavity walls systems representative of the Groningen building stock. *Report EUC318/2015U*, Eucentre, Pavia, Italy.
- Graziotti, F., Tomassetti, U., Rossi, A., Guerrini, G., Marchesi, B., Kallioras, S., Mandirola, M., Kouris, A., Penna, A., Magenes, G. 2016. Experimental campaign on a clay URM full-scale specimen representative of the Groningen building stock. *Report EUC128/2016U*, Eucentre, Pavia, Italy.
- Jafari, S., Panoutsopoulou, L. and Rots, J.G. 2015. Tests for the characterisation of original Groningen masonry, *Final report*, Delft University of Technology.
- de Normalisation, C. E. 2005. Eurocode 6: Design of Masonry Structures—Part 1-1: General Rules for Reinforced and Unreinforced Masonry Structures. Brussels, Belgium.
- Kasten, D., Schubert, P. 1985 Verblendschalen aus Kalksandsteinen: Beanspruchung, rissfreie Wandlänge, Hinweise zur Ausflührung. *Bautechnik* (3): 86-94 (in German).
- Kraus, J. 2014. Sequentially linear modelling of combined tension/compression failure in masonry structures. *MSc thesis report*, Structural Mechanics, TU Delft.
- Lemos, J.V. 2007. Discrete element modeling of masonry structures. *Int. J. Arch. Herit.* 1, 190-213.
- Lofti, H.R., Shing B.P. 1994. Interface model applied to fracture in masonry structures. *J. Struct. Eng.* 120, 63-80.
- Lourenco, P.B., Rots, J.G. 1997. Multisurface interface model for analysis of masonry structures. *J. Eng. Mech.* 123(7), 660-668.
- Lourenco, P.B., Rots, J.G., Blaauwendraad, J. 1998. Continuum model for masonry: parameter estimation and validation. *J. Struct. Eng.* 124(6), 642-652.
- Lourenço, P. B., Milani, G. 2014. Homogenization and Seismic Assessment: Review and Recent Trends. In *Mech. Mas. Struct.* (pp. 293-341). Vienna: Springer.
- Mendes, N., Lourenco, P.B. 2009. Seismic assessment of masonry “Gaioleiro” buildings in Lisbon, Portugal. *J. Earthq. Eng.* 14(1), 80-101.
- Milani, G., Valente, M. 2015. Failure analysis of seven churches severely damaged during the 2012 Emilia-Romagna earthquake: Nnolinear dynamic analysis vs. conventional approaches. *Eng. Failure Analysis* 54, 13-56.
- Pela, L., Cervera, M., Roca, P. 2012. An orthotropic damage model for the analysis of masonry structures. *Constr. Build. Mater.* 41, 957-967.
- Penna, A., Lagomarsino, S., Galasco, A. 2014. A nonlinear macroelement for the seismic analysis of masonry buildings. *Earthq. Eng. Struct. Dyn.* 43(2), 159-179.
- Ravenshorst, G., Esposito, R., Schipper, R. 2016. Quasi-static cyclic pushover test on the assembled masonry structure at TU Delft, *Preliminary report 3 February 2016*, Delft University of Technology.
- Ravenshorst, G., Messali, F., 2016a. In-of-plane tests on replicated masonry walls. *Final report*, Delft University of Technology.
- Ravenshorst, G., Messali, F., 2016b. Out-of-plane tests on replicated masonry walls. *Final report*, Delft University of Technology.
- Roca, P., Cervera, M., Gariup, G., Pela, L. 2010. Structural analysis of masonry historical constructions. Classical and advanced approaches. *Arch. Comput. Methods Eng.* 17, 299-325.
- Rots, J.G. (Ed.), Van der Pluijm, R. Vermeltfoort, A.Th., Janssen, H.J.M. 1994. *Structural masonry: an experimental-numerical basis for practical design rules*. Dutch version CUR report 171, English version 1997 Balkema, Rotterdam, 152 pp.
- Rots, J.G., Invernizzi, S. 2004. Regularized sequentially linear saw-tooth softening model. *Int. J. Num. Anal. Methods Geomech.* 28(78), 821-856.
- Rots, J.G., Hendriks, M.A.N. 2015. Elastic-brittle fraction model for robust post-peak analysis of masonry structures. *Key Eng. Materials* 624, 27-39, Proc. 4th Int. Conf. Mechanics of masonry structures strengthened with composite materials, MuRiCo 2014.
- Smoljanovic, H., Nikolic, Z., Zivaljic, N. 2015. A combined finite-discrete numerical model for analysis of masonry structures. *Eng. Fract. Mech.* 136, 1-14.